

# 3D Printing of Delicately Controllable Cellular Nanocomposites Based on Polylactic Acid Incorporating Graphene/Carbon Nanotube Hybrids for Efficient Electromagnetic Interference Shielding

Shaohong Shi, Zilin Peng, Jingjing Jing, Lu Yang, and Yinghong Chen\*



Cite This: *ACS Sustainable Chem. Eng.* 2020, 8, 7962–7972



Read Online

ACCESS |



Metrics & More



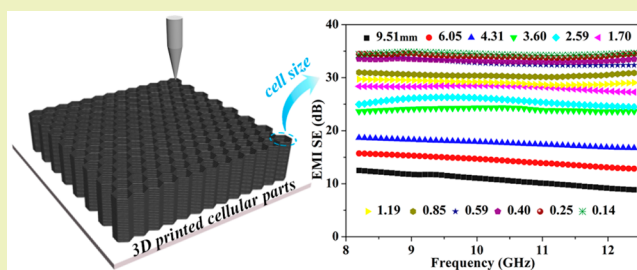
Article Recommendations



Supporting Information

**ABSTRACT:** Control of the architectures of three-dimensional (3D)-printed cellular parts to achieve electromagnetic interference (EMI) shielding protection is a challenging issue. In this paper, by combining FDM 3D-printing technology with hybridizing strategy, we successfully designed and fabricated high-performance polylactic acid nanocomposites incorporating graphene/carbon nanotube hybrids (PLA/GNPs/CNTs) and delicately controllable 3D-printed cellular parts. PLA/GNPs/CNTs nanocomposites prepared under the optimum conditions possessed the excellent comprehensive performance: Their tensile strength and Young's modulus can achieve values 16.2 and 25.5% higher than those of pure PLA, respectively. The corresponding electrical conductivity can reach 82.0 S/m, and EMI shielding efficiency can achieve 36.8 dB, which is far beyond the commercial shielding standard (20 dB). In addition, the 3D-printed cellular parts were successfully fabricated with light weight and highly efficient EMI shielding property. Finally, a cellular factor ( $T_{\text{cell}}$ ) was innovatively adopted to quantitatively evaluate the relationship between cell structures and EMI shielding behaviors of 3D-printed cellular materials, indicating that the critical cell size of about 4.29 mm could be successfully fitted to maintain the suitable shielding efficiency in X-band frequency range. These related investigations provide a new theoretical mechanism for evaluating the EMI shielding performance of 3D-printed cellular materials and open up new spaces for construction of the lightweight and multifunctional cellular parts for EMI protection applications.

**KEYWORDS:** 3D printing, Cellular materials, Polylactic acid, Graphene, Carbon nanotube, Electromagnetic interference shielding



## INTRODUCTION

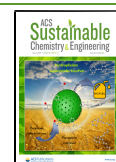
Cellular materials, composed of interconnected beams forming a complicated three-dimensional (3D) network framework,<sup>1</sup> represent the development trend of new materials with hierarchical and multifunctional structures. They possess the potential applications in various fields, such as energy absorption,<sup>2,3</sup> thermal insulation,<sup>4</sup> tissue engineering,<sup>5</sup> and wave attenuation.<sup>6,7</sup> The inspiration for design of these cellular materials is derived from the architecture of biomaterials in nature.<sup>8</sup> One of the representative cellular materials is honeycomb, which is composed of uniformly distributed hexagonal cells. These structures possess many advantages, such as light weight, high stiffness, and high specific surface area.<sup>9</sup> However, cellular biomaterials have been formed over thousands of years to achieve structurally and functionally optimized architectures. For traditional processing technologies such as extrusion and injection molding, it is very difficult to build these complicated structures.<sup>8</sup> Benefitting from the development of 3D-printing (additive manufacturing) technologies, there could be some new possibilities for us to fabricate the cellular structures by utilizing a new style of “layer-by-layer stacking” approach.<sup>10–12</sup> Many novel 3D-printed cellular structures have been successfully designed

and fabricated.<sup>13–16</sup> Obviously, 3D-printing technologies have overcome the restriction of traditional processing technologies by which means it is difficult to prepare the cellular materials with complicated architecture. However, with increasing demand for cellular materials, much attention is not only paid to construct the desired structures but also to maintain their excellent mechanical properties and functionalities, thus meeting the specific requirements in various fields.<sup>17,18</sup> For instance, some cellular materials were even particularly designed for the prevention of electromagnetic radiation pollution, because the involved special cellular structures can effectively block the propagation of electromagnetic waves. However, some cellular materials prepared by pure polymer generally cannot satisfy the requirement of EMI shielding applications, since they usually have weak EMI shielding

Received: March 7, 2020

Revised: May 3, 2020

Published: May 8, 2020



performance, e.g., polylactic acid (PLA) generally exhibits the transparent property for electromagnetic waves. This obviously hinders the development of cellular materials in EMI shielding applications. How to overcome this challenge and realize the required functionality and performance of materials for EMI shielding will be the topic deeply involved in this paper.

The primary purpose is to give the polymer materials with efficient EMI shielding property. In preparation of EMI shielding materials by the traditional processing technologies, adding carbon nanofillers into polymer matrix is one of the feasible methods.<sup>19–22</sup> As a representative of carbon nanofillers, graphene nanoplates (GNPs) are commonly used in electromagnetic radiation protection due to their excellent EMI shielding efficiency.<sup>23–26</sup> For instance, Zhai et al.<sup>24</sup> prepared the PEI/graphene nanocomposites (PEI/GNPs) with a GNPs loading of 10 wt % which exhibited the EMI shielding property of approximately 20 dB. Li et al.<sup>25</sup> fabricated the functionalized graphene sheets/PS (FGS/PS) composites with a porous structure, achieving a 29 dB EMI shielding effectiveness upon adding 30 wt % FGS. Apparently, the high loading of GNPs endows the materials with efficient EMI shielding property. However, we also noticed that there is a “mechanical percolation” phenomenon in GNPs-modified polymer systems,<sup>27</sup> indicating a critical content of fillers existing there. As the loading is lower than this content, the increase of fillers would result in a significant improvement in mechanical properties, while a further increase of loading may weaken the efficiency of this mechanical improvement. Hence, it is a great challenge to coordinate the comprehensive performance of GNPs modified materials. To overcome the above challenge and prepare the desired materials, the multidimensional hybridization with the other different functional fillers could be an effective and easily operational strategy, e.g., hybridizing with 1D metal nanowire,<sup>28</sup> 1D carbon nanotubes,<sup>29–32</sup> or 2D-MXene.<sup>33,34</sup> These multidimensional hybrid filler networks would endow the materials with the expected excellent comprehensive performance. However, when the EMI shielding effectiveness is further evaluated among different hybrid fillers, the hybrids of 2D graphene nanoplates/1D carbon nanotubes (GNPs/CNTs) proved to exhibit significant advantages in achieving the high shielding performance of materials at a low filler loading due to their unique nanostructure and excellent electrical property.<sup>29–32</sup> For example, Lou et al.<sup>31</sup> realized the desired EMI shielding property for commercial application through preparation of PVA/GNPs/CNTs composites with only 1.5 wt % hybrids. Besides, Yan et al.<sup>32</sup> manipulated a segregated structure in the graphite/carbon nanotubes/UHMWPE composites with 4 wt % hybrids, achieving an EMI shielding property of 41.8 dB. As analyzed above, it is feasible to obtain the desired properties through tailoring the hybrids.

Therefore, we expect to combine FDM 3D-printing technology and multidimensional hybridizing strategy to fabricate the cellular parts with complicated architectures and realize excellent performance for EMI shielding application, such as electromagnetic radiation pollution control. So far, few studies have been focused on this related work, and some fundamental investigations need to be carried out, such as the evolution of the structures of hybrids during printing process, the printability of nanocomposites, and the electromagnetic wave-attenuation effect of cellular structures. Here, rooted in these thoughts, by manipulating the entanglement network structures of GNPs/CNTs hybrids in PLA matrix, we

successfully designed and fabricated the PLA/GNPs/CNTs nanocomposites and their 3D-printed parts with excellent comprehensive performance, such as high mechanical properties, excellent electrical conductivity, and good EMI shielding efficiency (SE). Furthermore, combined with finite element simulation (FES), the complicated viscoelastic flow behaviors of melts in the printing channel and the materials' printabilities were also investigated. With the assistance of FES, the cellular structures matched with the required functionality were successfully constructed through FDM 3D printing. To gain a clear understanding of the effect of structures on the EMI shielding property, a series of complicated architectures with various cell geometry and cell size were fabricated. In addition, a quantitative relationship between cell structures and EMI shielding property was established and the cellular factor ( $T_{\text{cell}}$ ) was first used to illustrate this relationship. Herein, we have successfully built a mechanism to theoretically evaluate EMI shielding behaviors of 3D-printed cellular materials, which open up new spaces for the fabrication of cellular materials with lightweight and multifunctionality for electromagnetic radiation protection.

## EXPERIMENTAL SECTION

**Materials.** PLA (Ingeo 6201D) as a sustainable polymer material with a melting temperature of 167 °C, were supplied by NatureWorks, LLC. GNPs (SE1233) with a specific surface area of 400–550 m<sup>2</sup>/g, were provided by The Sixth Element (Changzhou) Materials Technology Co., Ltd., China. CNTs (NC7000) with an average length of 1.5 μm and diameter of 9.5 nm, were obtained from Nanocyl S.A., Belgium.

**Fabrication of PLA/GNPs/CNTs Nanocomposites and FDM 3D-Printed Parts.** Figure 1 provides a schematic diagram for

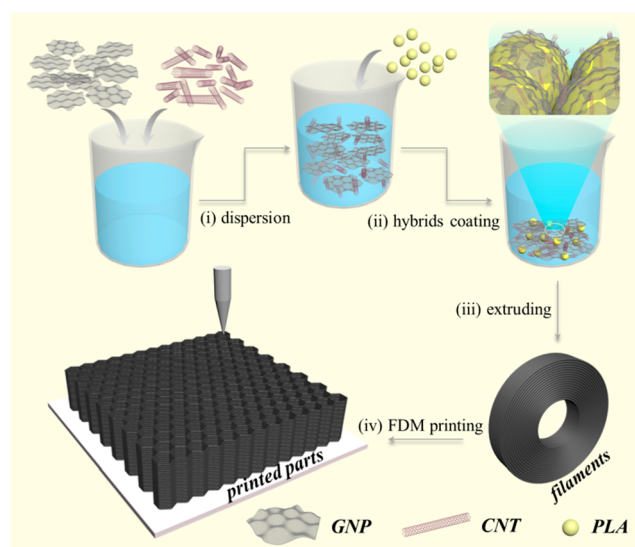


**Figure 1.** Schematic diagram for fabrication of PLA/GNPs/CNTs nanocomposites and FDM 3D-printed parts.

fabrication of PLA/GNPs/CNTs nanocomposites and FDM 3D-printed parts. First, a facile and green method of aqueous solution-deposition was used to prepare the GNPs/CNTs hybrid coated PLA particles. A certain amount of GNPs/CNTs hybrids in various weight ratio (GNPs/CNTs = 2/0, 2/0.5, 2/1, 2/2, and 2/4) was dispersed into deionized water under mechanical stirring (600 rpm) and ultrasonic treatment for 3 h to achieve a GNPs/CNTs hybrid suspension. The characterization of the dispersion and stability of above suspension was shown in Figure S1. It can be seen that the



good dispersion and stability of the suspension can still be maintained after standing for 30 min, which lays a good foundation for homogeneous coating of hybrid fillers on the surface of PLA particles. It is worth noting that the GNPs loading is strictly fixed (here 2 wt %) in the range of mechanical threshold<sup>27</sup> to achieve the best mechanical improvement (more evidence about the percolation threshold networks of GNPs was presented in Figure S2). In addition, the increase of CNTs content is mainly used to enhance the filler network. Then, a proper amount of PLA particles were added into the GNPs/CNTs hybrid suspension. The obtained mixture was stirred slowly for 1 h to let the hybrids adequately coat the surface of particles and then filtered with Buchner funnel. After drying, the GNPs/CNTs hybrid coated PLA particles were extruded into filaments suitable for FDM 3D printing by a single-screw extruder (RM-200C, Harbin HAPRO Electric Technology Co., Ltd., China) at 180 °C under a low-shear field. Thus, the PLA/GNPs/CNTs nanocomposite filaments were successfully prepared for the next step. For convenient description, the obtained PLA/GNPs/CNTs nanocomposites were named as PLA2/0, PLA2/0.5, PLA2/1, PLA2/2, and PLA2/4, respectively, where “PLA $m/n$ ” indicates that the prepared PLA filament contains  $m$  wt % GNPs and  $n$  wt % CNTs. Finally, the fabrication of FDM 3D-printed parts was finished on a standard open-air desktop printer (German RepRap X350pro, Feldkirchen, Germany) by using the prior prepared filaments. More FDM 3D-printing parameters were illustrated in Table S1.

**Characterization.** Scanning electron microscopy (SEM) was carried out using an FEI Inspect apparatus (FEI Co., Ltd., USA) with an acceleration voltage of 20 kV to investigate the surface morphology of PLA particles before and after being coated with GNPs/CNTs hybrids. Moreover, the fractured surfaces of FDM 3D-printed samples after tensile tests were observed to reveal the fracture mechanism. The morphology of FDM 3D-printed cellular structures with different cell geometry was also observed. A laser-scattering particle size analyzer (Microtrac S3500-SI, USA) was applied to analyze the size distribution of PLA particles. A Nicolet 6700 FTIR spectrometer (Thermal Scientific, USA) was used to investigate the interaction between GNPs/CNTs hybrids and PLA particles in the wavenumber range of 4000–400  $\text{cm}^{-1}$ . A parallel-plate rotational rheometer (TA Instruments, USA) was used to investigate the rheological behaviors of PLA/GNPs/CNTs nanocomposites with a sample dimension of 25 mm diameter and 1 mm thickness. The frequency sweeps were performed at 190 °C in a frequency range of 0.01–100 Hz with a fixed strain of 5%. The steady shear sweeps were carried out at 190 °C within a shear rate range of 0.001–500  $\text{s}^{-1}$ . The distribution of GNPs/CNTs hybrids in PLA matrix was observed using transmission electron microscopy (TEM; JEOL JEM-100CX, Japan) on a copper grid with an accelerating voltage of 200 kV. Prior to observation, the samples were cryogenically cut into ~100 nm thin sections with a LEICA EM FC6 frozen ultramicrotome. The mechanical properties of the dumbbell-shaped samples (75 × 4 × 2  $\text{mm}^3$ ) prepared by both compression molding and FDM 3D printing were measured on a universal testing machine (Instron 5569, Instron Instruments, USA) with a cross-head speed of 10 mm/min and a gauge length of 20 mm. Five specimens were tested for the averaged values. A computerized Keithley 2400 SourceMeter (Keithley Instruments, USA) was employed to investigate the electrical property of the nanocomposites with sample dimensions of 1.75 mm diameter and 10 mm length. Prior to measurement, the two ends of filaments were covered with conductive silver glue to ensure good contact between the sample and the electrodes. For each sample, five measurements were conducted to obtain the averaged values. An Agilent N5230 vector network analyzer, equipped with an APC-7 connector as the coaxial test cell, was used to investigate the EMI shielding property of nanocomposites in X-band frequency range (8.2–12.4 GHz) and the FDM 3D-printed cellular parts with different cell geometries and cell sizes in the X- (8.2–12.4 GHz) and S-band (2.0–4.0 GHz) frequency ranges. All the measured samples have the same dimensions of 13 mm diameter and 2 mm thickness. The scattering parameters ( $S_{11}$  and  $S_{21}$ ) were recorded to calculate the EMI shielding parameters, including reflected power ( $R$ ), transmitted power ( $T$ ), absorbed power ( $A$ ),

EMI shielding ( $SE_{\text{total}}$ ), microwave reflection ( $SE_R$ ), microwave absorption ( $SE_A$ ), and microwave multiple internal reflection ( $SE_m$ , but generally if  $EMI SE_{\text{total}} \geq 10$  dB, it can be ignored). The related equations were given as follows:<sup>26</sup>

$$R = |S_{11}|^2 \quad (1)$$

$$T = |S_{21}|^2 \quad (2)$$

$$R + T + A = 1 \quad (3)$$

$$SE_A = 10 \lg \left( \frac{1}{1 - R} \right) \quad (4)$$

$$SE_R = 10 \lg \left( \frac{1 - R}{T} \right) \quad (5)$$

$$SE_{\text{total}} = SE_A + SE_R + SE_m \quad (6)$$

In order to simulate the complicated viscoelastic flow behaviors of polymer melts in the printing channel and to predict the processability of printing materials, commercial software POLYFLOWs 17.0 (ANSYS, Inc., USA) with an ICEM module for meshing the structured grid was employed for finite element calculations. More details about the simulation procedures were provided in Figure S3 and Table S2.

## RESULTS AND DISCUSSION

**Morphology of GNPs/CNTs Hybrid Coated PLA Particles.** To verify the successful coating of GNPs/CNTs hybrids on the surface of PLA particles by a solution-deposition method, the morphology was observed by SEM. As shown in Figure 2a, before coating, a uniform size

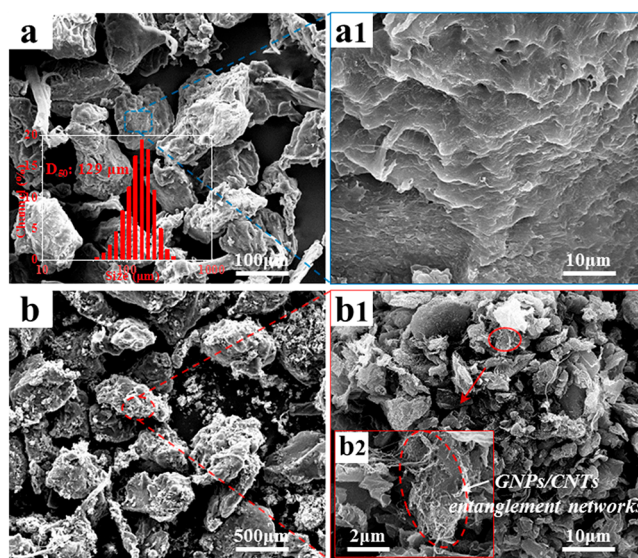


**Figure 2.** SEM images of PLA particles before (a, a1) and after (b, b2) being coated with GNPs/CNTs hybrids. The inset image shows the size distribution of PLA particles.

distribution of PLA particles is noticed, and the averaged particle size is statistically at about 129  $\mu\text{m}$  according to the particle size analysis results (Figure 2a, inset image). In the magnified SEM image (Figure 2a1), there are many rugged structures observed on the surface, which could provide a favorable condition for coating of GNPs/CNTs hybrids. As shown in Figure 2b, after coating, it is very clear that the surface becomes very rough, and there are many GNPs/CNTs hybrids firmly adhered to the surface (Figure 2b1,b2, with

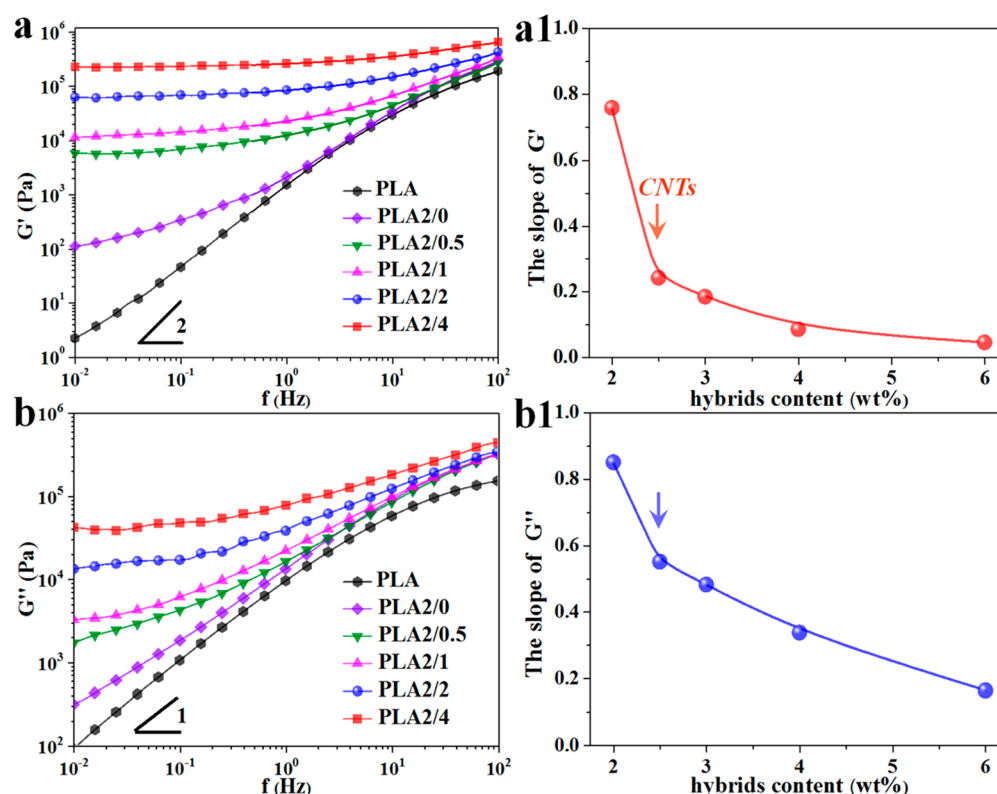


**Figure 3.** Storage modulus ( $G'$ ) (a), loss modulus ( $G''$ ) (b), and the corresponding terminal region slopes (a1, b1) of pure PLA and PLA/GNPs/CNTs nanocomposites.

higher magnification). To investigate the possible interactions between GNPs/CNTs hybrid fillers and PLA particles, FTIR measurement was conducted, and the results are shown in Figure S4. It can be seen that there are the possible hydrogen bonding physical interactions between GNPs/CNTs hybrids and PLA particles (the detailed analyses and illustrations are presented in the Supporting Information) after incorporating GNPs/CNTs hybrid fillers. That is to say, the hydrogen bonding physical interactions mentioned above and the possible physical adsorptions (the similar phenomena was also confirmed by our previous work)<sup>35</sup> could be the driving force to make GNPs/CNTs hybrid fillers coat on the surface of PLA particles. Meanwhile, the entanglement structures of hybrids are also found in Figure 2b2 (inset image). Obviously, plenty of CNTs are intersected by each other randomly like “feelers” and are firmly fixed on the GNPs surfaces. These structures could effectively increase the filler’s overlapping joints and broaden the contact areas, thus resulting in formation of strong filler networks in matrix. Then, the GNPs/CNTs hybrid coated PLA particles were extruded into filaments under the given conditions.

**Characterization of PLA/GNPs/CNTs Nanocomposites.** Furthermore, to reveal the possibility of forming GNPs/CNTs hybrid networks in the PLA matrix, the rheological behaviors of PLA/GNPs/CNTs nanocomposites were investigated. As shown in Figure 3a,b, upon introducing the GNPs/CNTs hybrids, both the storage modulus  $G'$  and loss modulus  $G''$  increase monotonically. Particularly based on the low-frequency viscoelastic response shown in Figure 3a1,b1, there is a homopolymer-like terminal flow behavior exhibiting on pure PLA, which shows a scaling property of approximately  $G' \sim \omega^2$  and  $G'' \sim \omega^1$ . This is mainly due to the

full relaxation of polymer molecular chains at the molten state.<sup>36,37</sup> After coating of GNPs/CNTs hybrids, this dependence weakens. For the PLA2/0 sample, the power law indexes obtained from  $G' \sim \omega$  and  $G'' \sim \omega$  curves decrease to 0.76 and 0.85, respectively, suggesting that the filler’s network structures have been preliminarily formed.<sup>36</sup> It is worth noting that a sudden jump appears in the viscoelastic response curves of  $G'$  and  $G''$  with incorporation of CNTs, even at low CNTs loading. For the PLA2/0.5 sample, the terminal flow behavior entirely disappears and the corresponding power-law index of  $G'$  sharply decreases to 0.24. Such a nonterminal behavior indicates that there is a transition appearing for material melts from liquid-like to solid-like ( $G' \sim \omega^a$ ,  $0.3 < a < 0$ ). The reason for this could be attributed to a better restraint effect of GNPs/CNTs hybrids on the motion of polymer chains.<sup>38</sup> With further increasing the hybrids content, the power law index of  $G'$  decreases to be lower than 0.2. This strong restraint for the polymer molecular chains implies that the strong hybrid networks exist in PLA matrix. The change trend of  $G''$  is similar to that of  $G'$ . Regarding the high-frequency response,  $G'$  and  $G''$  show similar frequency dependence for all samples and increase almost monotonically with frequency, suggesting that the GNPs/CNTs hybrids have little influence on the short-range dynamics of polymer molecular chains.

Although the existence of strong GNPs/CNTs hybrid networks has been proved by rheological characterizations, their micromorphology structures are still not clear enough. The TEM morphologies of two representative samples (PLA2/0 and PLA2/0.5) are highlighted in Figure 4. Clearly, for the PLA2/0 sample (Figure 4a,a1), the GNPs clusters are noticed in the PLA matrix, and the magnified TEM images reveal that the GNPs layers are closely connected with each other, thus



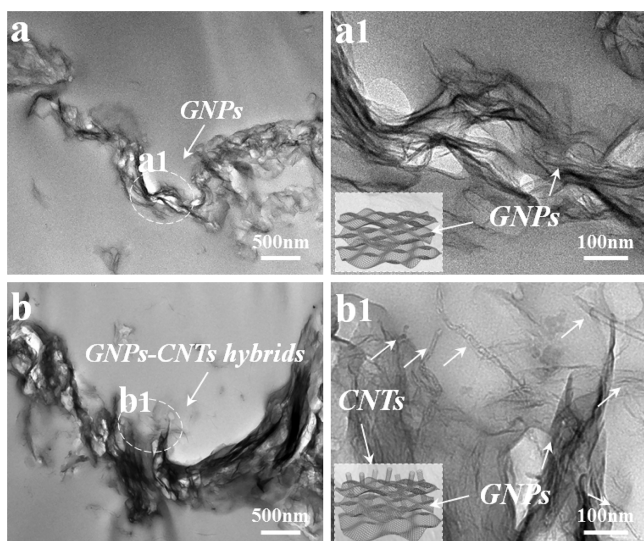


**Figure 4.** TEM images of PLA2/0 (a, a1) and PLA2/0.5 nanocomposites (b, b1).

constructing the network frameworks. As for the PLA2/0.5 sample (Figure 4b,b1), besides the GNPs networks, the entanglement structures between GNPs and CNTs are also observed. Apparently, the feeler-like CNTs are firmly caught on the GNP surface and intersected each other. The TEM observations again verify that there are really the entanglement structures in PLA matrix, which interlock with each other. This could also explain well the reason for the sudden change in rheological behavior. Therefore, up to now we have gained a clear understanding of the macroscopic and microscopic structures of GNPs/CNTs hybrids in PLA matrix.

On the basis of previous investigations, we continue to explore the properties of the PLA/GNPs/CNTs nanocomposites. The mechanical properties of the compression-molded PLA/GNPs/CNTs nanocomposites were investigated, and the representative stress–strain curves are shown in Figure 5. As expected, the GNPs/CNTs hybrids exhibit a positive influence on the mechanical performance of nanocomposites. For the PLA2/0 sample with only 2 wt % GNPs, the tensile strength achieves 58.0 MPa, while that of the pure PLA sample is 53.1 MPa. That is, the former shows the 9.2% improvement over the latter, and the Young's modulus shows the same trend as the tensile strength. The reason for this improvement is that there would be better compatibility between GNPs and PLA matrix when the filler content is near the mechanical

threshold,<sup>27</sup> thus achieving a mechanical improvement. Furthermore, with the incorporation of GNPs/CNTs hybrids, the nanocomposites exhibit an enhancing tendency in the mechanical properties. Particularly for the PLA2/4 sample, the tensile strength and Young's modulus optimally increase to 61.7 and 3450 MPa, respectively. Relative to pure PLA, the increase degree reaches 16.2% for tensile strength and 25.5% for Young's modulus, respectively. Obviously, it is encouraging that the combination of GNPs/CNTs hybrids is advantageous to the substantial enhancement in mechanical properties. Regarding the enhancement mechanism, it is believed that this is mainly because the CNTs intersect the GNP layers, decreasing the van der Waals forces occurring between GNP layers and preventing the stacking of GNPs.<sup>31,39,40</sup> Therefore, the mechanical properties (mainly tensile strength) of nanocomposites mainly show a monotonically increasing tendency with the hybrids content increasing.

The functionalities of the PLA/GNPs/CNTs nanocomposites were further investigated. Figure 6 shows the electrical conductivity and EMI shielding property of the nanocomposites. Clearly, as shown in Figure 6a, the GNPs/CNTs hybrids exhibit a positive influence on improving the electrical conductivity. For the PLA2/0 sample, the electrical conductivity reaches approximately 0.04 S/m, indicating the transition of nanocomposites from insulator to conductor and the preliminary formation of conductive networks in the matrix.<sup>41</sup> Upon incorporation of CNTs, like the rheological behavior, a significant improvement is noticed even at only 0.5 wt % CNT loading. The electrical conductivity of the PLA2/0.5 sample is 2 orders of magnitude higher than that of the sample without CNTs (PLA2/0). Such an enhancement further confirms that the entanglement networks of GNPs/CNTs hybrids surely play an important role in the improvement of electrical property. With a further increase of CNTs loading, the electrical conductivity still presents a continuous increasing tendency. As the CNTs loading increases to 4 wt %, the electrical conductivity also increases to 82.0 S/m, suggesting that strong conductive networks have been successfully constructed. Generally speaking, for the electrical conductive composites, the high electrical conductivity often leads to the efficient EMI shielding property.<sup>22,42</sup> Accordingly, the corresponding EMI shielding properties of PLA/GNPs/CNTs nanocomposites in X-band frequency range are evaluated and the results are provided in Figure 6b. As expected, the entanglement networks of GNPs/CNTs hybrids effectively impart the high shielding property to the nanocomposites. For instance, for PLA2/1 sample with only 1 wt %

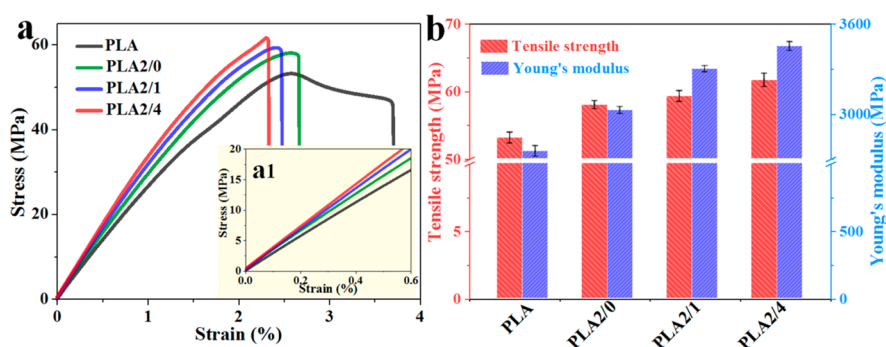


**Figure 5.** Representative stress–strain curves (a, a1) and corresponding tensile strength and Young's modulus of the compression-molded PLA/GNPs/CNTs nanocomposites (b).

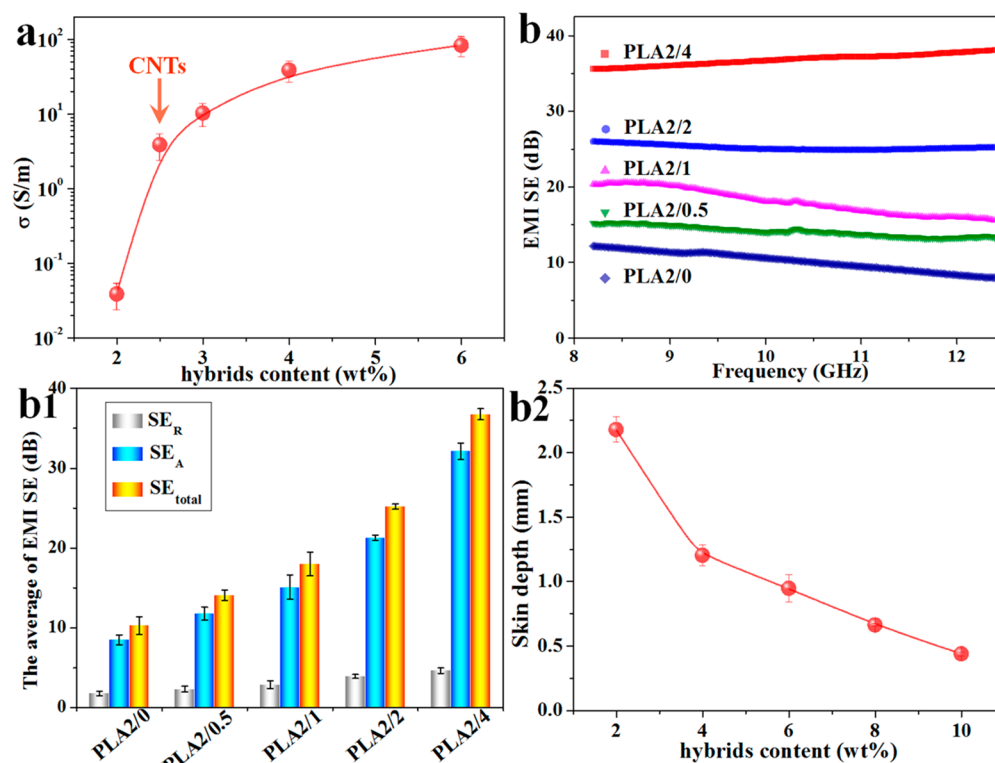


**Figure 6.** Electrical conductivity (a) and EMI shielding property (b) of PLA/GNPs/CNTs nanocomposites; the corresponding EMI shielding parameters including  $SE_{total}$ ,  $SE_R$ , and  $SE_A$  (b1) and skin depth (b2).

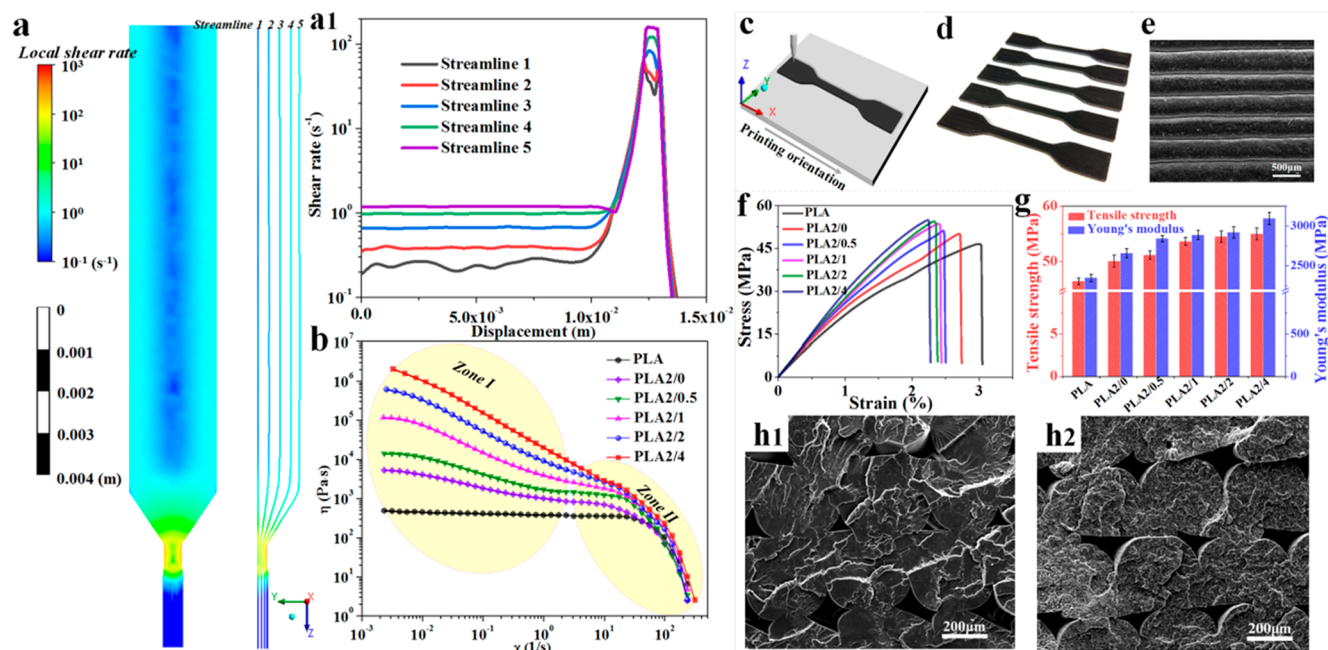


**Figure 7.** Shear rate distribution of polymer melts on the symmetry plane of whole liquefier channel (a) and the shear rate curves with 5 equally spaced streamlines on the half of  $Y-Z$  planes along the  $+Z$  direction (a1); apparent viscosity of pure PLA and PLA/GNPs/CNTs nanocomposites as a function of shear rate (b); schematic diagram of dumbbell-shaped model for 3D printing (c); digital images of the FDM 3D-printed dumbbell-shaped parts (d) and the corresponding SEM image of top surface of these samples (e); representative stress–strain curves of the FDM 3D-printed dumbbell-shaped parts and the corresponding mechanical properties (f, g); SEM images of the fractured surfaces of pure PLA (h1) and PLA2/2 (h2) samples after tensile test.

CNTs loading, its EMI SE could increase to 20 dB at 9 GHz, which preliminarily satisfies the requirement of commercial shielding standard (20 dB).<sup>32,43</sup> As the CNTs content further

increases to 2 and 4 wt %, the EMI SE is also increases to 25.2 and 36.8 dB, respectively, which is far beyond the commercial standard. This encouraging result indicates that through

GNPs/CNTs synergism, CNTs loading optimization, and hybrids coating, PLA/GNPs/CNTs nanocomposites with excellent EMI shielding property have been finally obtained. Furthermore, the EMI shielding mechanism of these nanocomposites is revealed by the corresponding EMI shielding parameters ( $SE_{total}$ ,  $SE_R$ , and  $SE_A$ ). As shown in Figure 6b1,  $SE_{total}$  and  $SE_A$  show the monotonic enhancement with increase of the loading of GNPs/CNTs hybrids, while  $SE_R$  basically exhibits little change. The above phenomenon strongly demonstrates that the absorption of electromagnetic waves dominantly works in the shielding mechanism of GNPs/CNTs hybrids filled materials. As the electromagnetic waves penetrate into the interior of materials, the conductive networks would block their spreading, thus increasing the internal multiple reflections. In this process, the electromagnetic energy would be converted to Joule heat, dissipating in the air.<sup>32,44</sup> In addition, another parameter of skin depth is also employed to explore the shielding mechanism. As shown in Figure 6b2, the similar trend also reveals that the depth decreases with increase of the hybrids loading. The reason for this is that the strong hybrid networks increase the internal multiple reflections of incident electromagnetic waves, resulting in high energy loss. Therefore, the energy could quickly decay to  $1/e$ . Here, we have adopted two electromagnetic parameters to successfully reveal the EMI shielding mechanism of the PLA/GNPs/CNTs nanocomposites toward electromagnetic waves. Accordingly, we have prepared PLA/GNPs/CNTs nanocomposites with excellent mechanical property, electrical conductivity, and EMI shielding performance through the GNPs/CNTs hybridizing strategy, which are suitable for FDM 3D printing. In the following, cellular structures will be realized through FDM 3D printing of the above high-performance and multifunctional nanocomposites.

**Fabrication and Characterization of FDM 3D-Printed Cellular Parts.** From materials to 3D-printed parts, there are still some difficulties needing to be overcome, e.g., do the previously prepared nanocomposites possess the 3D printability? Do the original material performances change after FDM 3D printing? Actually, these questions are essentially related to the fluid dynamics of polymer melts in the printing channel. Here, finite element simulation (FES) was employed to analyze the fluid dynamics of polymer melts. The profiles of shear rate distributions are shown in Figure 7a. Apparently, the shear rate distribution is uniform throughout the whole channel. In order to understand the flowing mechanism of polymer melts, the shear rate distributions represented by the five equally spaced streamlines located on the half of  $Y-Z$  planes along  $+Z$  direction are exhibited in Figure 7a1. In the whole liquefying process, the melts show a steady flow. At the beginning, the melts exhibit a low shear rate. When the melts arrive in the convergence zone, the shear rate performs a significant increase. After reaching the maximum, the melts smoothly leave out of the exit. There is no obvious “turbulent flow” phenomenon occurring in the liquefier channel. Compared the various streamlines, their common characteristics of steady flow could be revealed, as follows: (1) In the same region ( $Y-Z$  planes) along  $+Z$  direction, the profile of each streamline is similar. (2) There is a low shear rate in the range of  $10^0$ – $10^3$   $s^{-1}$ , where the maximum one is only at 808  $s^{-1}$  (far less than the shear rate occurring in traditional extrusion or injection molding). Therefore, the melt flow in the whole liquefier channel is thought to be steady, i.e., the GNPs/CNTs hybrid networks would be kept after printing. This is

very important for fabricating high-performance functional parts after FDM 3D printing. Our further experimental results show that the EMI shielding property of the 3D-printed parts could be still retained at 35.5 dB, which exhibits almost no change after printing (the result is provided in Figure S5). Hence, based on the numerical simulations and experimental results, it can be concluded that the prepared PLA nanocomposites incorporating GNPs/CNTs hybrids could still keep their high performance and excellent functionality after FDM 3D printing. In addition, we also investigate the printability of the nanocomposites. Figure 7b shows the apparent viscosity of pure PLA and PLA/GNPs/CNTs nanocomposites as a function of shear rate. Apparently, the curves are divided into two zones (I and II). In zone I (with shear rate lower than  $10^0$   $s^{-1}$ ), a typical Newtonian-flow characteristic is observed for pure PLA sample, while a shear-thinning behavior is observed for the other samples. The reason for this could be due to the confinement effect of GNPs/CNTs hybrids on the polymer molecular chains at low shear rate.<sup>37</sup> In zone II, all samples show the similar shear rate dependence, i.e., no matter whether pure PLA or PLA/GNPs/CNTs nanocomposites, they both exhibit the similar rheological behavior (melt processability). Coincidentally, in this zone the shear rate distribution is consistent with that of the simulation result in printing channel (Figure 7a1). The above results indicate that all of the prepared GNPs/CNTs hybrids filled materials could be printable.

The prior prepared PLA/GNPs/CNTs nanocomposite filaments were applied for fabrication of the FDM 3D-printed parts. First, the corresponding mechanical properties were investigated. The dumbbell-shaped part model with a dimension of  $75 \times 4 \times 2$  mm<sup>3</sup> for 3D printing was generated by Pro/Engineer 5.0, and the schematic profile of sample is shown in Figure 7c. The representative FDM 3D-printed dumbbell-shaped parts and the corresponding SEM image of the top surfaces of these samples are highlighted in Figure 7d,e, respectively. The distribution of the homogeneously deposited filaments and their good interfacial combination can be clearly observed, which could guarantee the required mechanical properties. The representative stress–strain curves of the 3D-printed dumbbell-shaped samples and the corresponding mechanical performance comparison are performed in Figure 7f,g. Here, it should be explained that all samples for mechanical test were prepared by FDM 3D printing (however, all samples used in Figure 5 are prepared by compression molding). Obviously, the tensile strength and Young's modulus of the 3D-printed parts exhibit an increasing tendency with the introduction of the GNPs/CNTs hybrids. Particularly, the tensile strength of the PLA2/4 part achieves 55.0 MPa, which is much higher than that of the pure PLA part (46.5 MPa) and the PLA2/0 part (50.1 MPa). Obviously, the GNPs/CNTs hybrids play an important role in imparting the obviously enhanced mechanical performance to FDM 3D-printed parts. Figure 7h1,h2 compare the SEM morphologies of the 3D-printed samples of pure PLA and PLA2/2 nanocomposite samples after tensile test. It can be seen that after tensile test the cross section of the deposited pure PLA sample deforms a lot, but the cross section of the regularly deposited PLA2/2 nanocomposite sample basically does not deform as compared with the former. The reason for the good deformation resistance of nanocomposites could be attributed to the reinforcing effect of the GNPs/CNTs hybrids. In addition, it is worth noting that a decrease of the mechanical properties for



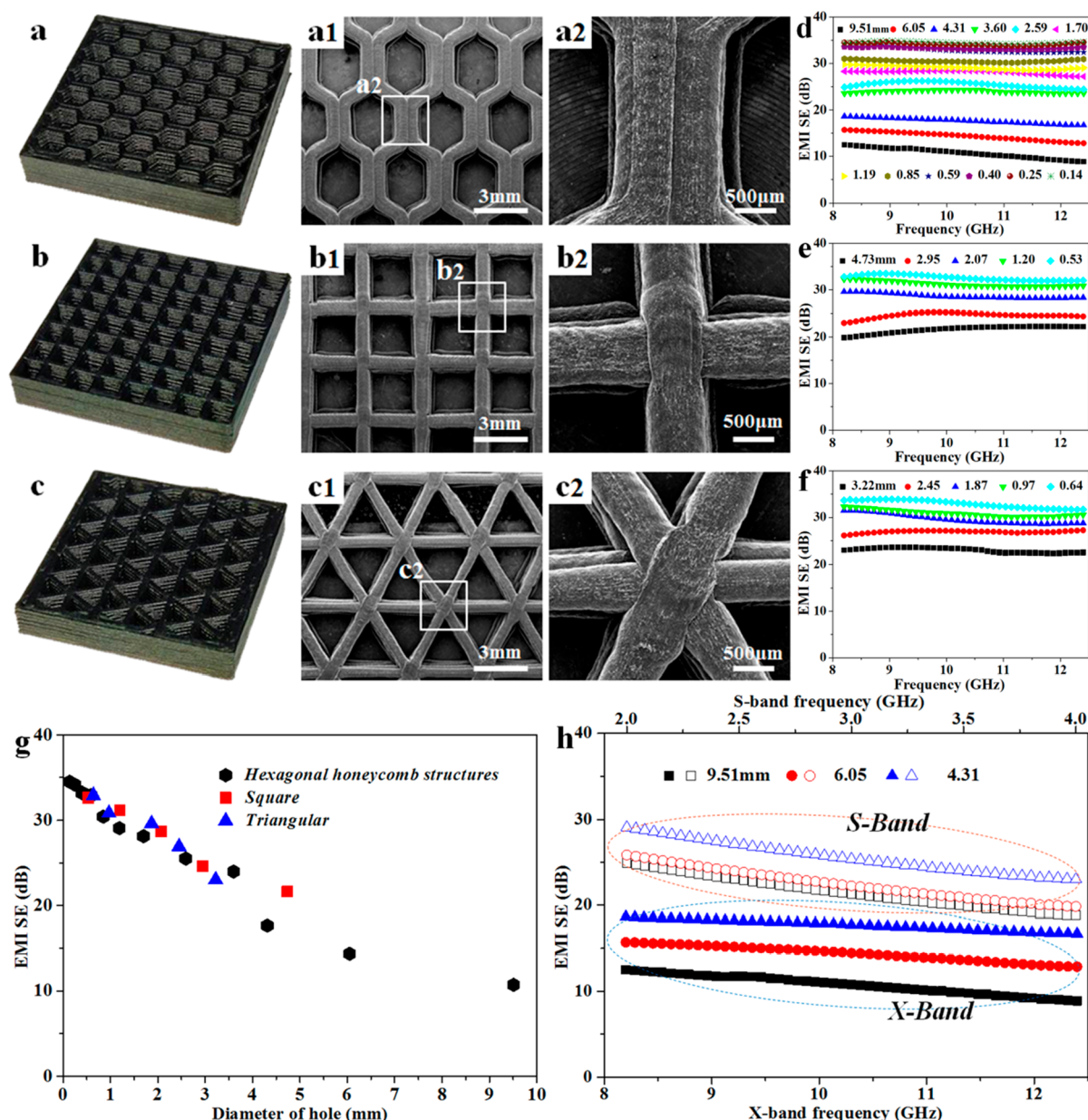


**Figure 8.** Representative digital images and SEM photos of FDM 3D-printed cellular honeycomb-like structures with various cell geometry: hexagon (a, a2), square (b, b2) and triangle (c, c2); EMI shielding property of 3D-printed parts with different cellular structures of different cell size: hexagon (d), square (e), and triangle (f) in X-band frequency range; average EMI SE of 3D-printed parts with different cellular geometry as a function of cell size (g); EMI shielding property of 3D-printed parts with hexagonal cellular structures of different cell size in X- and S-band frequency ranges (h).

all printed samples prepared by FDM 3D-printing technology is noticed after printing. It is mainly due to the holes distributed on the interface of layers (as shown in Figure 7h1,h2), resulting in the decrease as compared with the traditional compression-molded sample (without holes). After evaluating the comprehensive performance of all samples, the PLA2/4 nanocomposite has the best electromagnetic and mechanical properties; hence, its filament is selected to prepare the cellular electromagnetic interference shielding parts.

To prepare the EMI-shielding cellular 3D-printed parts, the honeycomb-like architectures with different cell geometries (hexagon, square, and triangle) were constructed. The representative cellular structures printed with the PLA2/4 nanocomposite are shown in Figure 8a–c. As the digital

photos show, the cellular 3D-printed parts with a larger dimension (thickness of 4 mm and length of 40 mm) were successfully fabricated. To have a clearer observation of these cellular structures, the SEM morphologies of the microstructures of these architectures were provided (Figure 8a1–c1 at a lower magnification and Figure 8a2–c2 at a higher magnification). Obviously, for each sample, the regular and well-defined cellular structures are clearly presented. At a higher magnification (Figure 8a2–c2), the cell walls in between are tightly bound, suggesting a good coalescence of the printing filaments during deposition. Furthermore, to evaluate the effect of cell geometry and cell size on the EMI shielding property, the measurements of EMI shielding were carried out on the cellular 3D-printed parts with different cell

size and cell geometry. The results are shown in Figure 8d–f. Simultaneously, the representative FDM 3D-printed models and the corresponding digital images of the FDM 3D-printed parts with different cell size and cell geometry are exhibited in Figure S6. It can be seen that there is a similar tendency occurring in all the cellular 3D-printed parts with different cell geometry, i.e., the EMI SE decreases with decreasing the cell size. However, there is also the difference in the EMI shielding property between different cell geometries. The influence of the cell size and cell geometry on the averaged EMI SE is exhibited in Figure 8g. It is clearly seen that the EMI shielding properties of the cellular 3D-printed parts are mainly affected by the cell size and the influence of the cell geometry could be negligible. The reason for this could be attributed to the transmission pattern of the electromagnetic waves. Similar to sound or light waves, electromagnetic waves easily pass through the hole as the size of the wavelength is smaller than that of the hole. Here, the cell size is close to the wavelength in the X-band frequency range (24~48 mm). Therefore, the EMI shielding properties exhibit a much stronger dependence on the cell size than on the cell geometry. To further verify this conclusion, the EMI shielding behaviors of the hexagonal honeycomb-like 3D-printed samples with the specified cell size were examined in different frequency ranges, including the X-band range of 24~36 mm and S-band range of 48~100 mm. As we expected, for the same sample, a longer wavelength would lead to a relatively higher EMI shielding property. For instance, the averaged EMI SE of sample with 4.31 mm cell size is at about 25.7 dB in the S-band frequency range, while at only about 17.7 dB in the X-band frequency range. A similar tendency is noticed in other different cell sizes. The above results adequately indicate that the cell size of cellular 3D-printed parts plays a dominant role in controlling the EMI shielding property.

To quantify this relationship between cell size and EMI shielding property, the shielding mechanism was first explored. As we know, the cell size directly affects the transmission coefficient of electromagnetic waves. The relationship between EMI shielding property and transmission coefficient obeys the following equation:<sup>43</sup>

$$\text{EMI SE} = 20 \lg \frac{1}{T} \quad (7)$$

where EMI SE represents the EMI shielding property of materials and  $T$  represents the intrinsic transmission coefficient of materials, reflecting the capability of electromagnetic waves to permeate materials. However, above law is mainly used to evaluate materials without any cellular structure. In this study, a cellular factor ( $T_{\text{cell}}$ ) is introduced to describe the effect of cellular structure on the shielding property. The modified  $T_{\text{total}}$  is the transmission coefficient of cellular material and is equal to the sum of the contributions of the transmission coefficient of materials without hole ( $T$ ) and the cellular factor ( $T_{\text{cell}}$ ):

$$T_{\text{total}} = T + T_{\text{cell}} \quad (8)$$

where  $T_{\text{cell}}$  represents the corresponding cellular factor. Accordingly, eq 8 can be modified as follows:

$$\text{EMI SE} = 20 \lg \frac{1}{T + T_{\text{cell}}} \quad (9)$$

Obviously, based on above modified eq 9,  $T_{\text{cell}}$  could be successfully obtained. As a result, the influence of cell size on the EMI shielding property can be easily quantified.

Furthermore, a dimensionless factor ( $\mu$ ) is applied to evaluate the relationship between intrinsic transmission coefficient ( $T$ ) and cellular factor ( $T_{\text{cell}}$ ). The equation is given as follows:

$$\mu = \frac{T_{\text{cell}}}{T} \quad (10)$$

The  $\mu$  was plotted as a function of cell size in the X-band range, and the result is shown in Figure 9. Clearly, when the

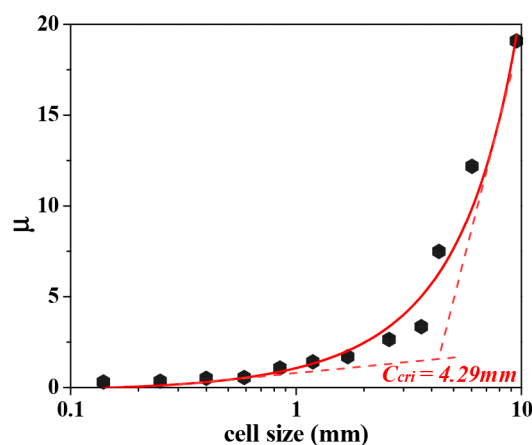


**Figure 9.** Ratio of cellular factor to intrinsic transmission coefficient of FDM 3D-printed cellular structures ( $\mu$ ) as a function of cell size in X-band frequency range.

cell size is small ( $<1.7$  mm), the change in  $\mu$  is also very small, indicating a weak effect on the EMI shielding property. With a further increase of the cell size, a sharp increase is noticed, suggesting that the effect of cell size on the EMI shielding property cannot be neglected. To illustrate this transition, a critical cell size ( $C_{\text{crit}}$ ) was proposed and then calculated. As shown in Figure 9, this  $C_{\text{crit}}$  is determined to be about 4.29 mm. Obviously, in the X-band frequency range, below the critical cell size ( $C_{\text{crit}}$ ), the effect of cell size on the shielding property is weak and the cellular 3D-printed parts exhibit good shielding property toward the electromagnetic waves. However, above  $C_{\text{crit}}$ , the influence of the cell structures cannot be neglected. Masses of electromagnetic waves would be transmitted to the materials, thus weakening the efficiency of the shielding property. So far, we have successfully determined the relationship between 3D-printed cellular structure and EMI shielding property, thus making it possible to design and fabricate a wide range of cellular materials with delicately controllable architecture and functionality through 3D-printing strategy for electromagnetic radiation pollution control.

## CONCLUSIONS

In summary, in order to effectively block the electromagnetic radiation, the delicately controllable 3D-printed cellular parts with light weight and highly efficient EMI shielding property were successfully designed and fabricated by combining FDM 3D-printing technology with a hybridizing strategy. To achieve the desired structures and functionalities, several challenges were overcome. First, by carefully manipulating and controlling the entanglement network structures of GNPs/CNTs hybrids, we successfully endowed the prepared PLA/GNPs/CNTs nanocomposites with high mechanical properties and excellent EMI shielding efficiency. Under the condition of the optimum formulations of nanocomposites, the corresponding tensile

strength and Young's modulus increase by 16.2 and 25.5%, respectively, as compared with those of pure PLA. In addition, the corresponding electrical conductivity reaches 82.0 S/m, and the EMI shielding property reaches 36.8 dB, which completely meets the requirements for the commercial shielding applications (at least 20 dB level). Furthermore, with the assistance of the finite element simulation on the fluid dynamics of polymer melts, the viscoelastic behaviors of polymer melts were carefully investigated, revealing the steady melt flow occurring in the printing liquefier channel. On this basis, the high-performance and multifunctional FDM 3D-printed cellular parts were fabricated, achieving optimum performance at loadings of 2 wt % graphene and 4 wt % carbon nanotube. Finally, the quantitative relationship between cell structures and shielding properties was successfully established, and a cellular factor ( $T_{\text{cell}}$ ) was introduced to coordinate this relationship for the first time. The related investigations could provide a new theoretical mechanism for evaluating the EMI shielding performance of 3D-printed cellular materials, thus opening up new spaces for the design and fabrication of cellular structures with light weight and multifunctionality to control the electromagnetic radiation pollution.

## ■ ASSOCIATED CONTENT

### Supporting Information

The Supporting Information is available free of charge at <https://pubs.acs.org/doi/10.1021/acssuschemeng.0c01877>.

Digital images of GNPs/CNTs hybrid suspension before and after standing for 30 min; polarized microscopy images of PLA/GNPs nanocomposites with different GNPs content; FDM printing parameters; detailed procedures for finite element simulation; geometry of whole printing channel and the corresponding mesh; intrinsic parameters of melts; FTIR spectra of PLA particles before and after incorporating GNPs/CNTs hybrids; EMI shielding property of PLA2/4 nanocomposites before and after printing in X-band frequency region; representative FDM 3D-printed models and corresponding digital images of printed-samples with different cell size in various cell geometries (PDF)

## ■ AUTHOR INFORMATION

### Corresponding Author

**Yinghong Chen** – State Key Laboratory of Polymer Materials Engineering, Polymer Research Institute of Sichuan University, Chengdu 610065, Sichuan, China; [orcid.org/0000-0003-2169-4673](https://orcid.org/0000-0003-2169-4673); Email: [johnchen@scu.edu.cn](mailto:johnchen@scu.edu.cn)

### Authors

**Shaohong Shi** – State Key Laboratory of Polymer Materials Engineering, Polymer Research Institute of Sichuan University, Chengdu 610065, Sichuan, China

**Zilin Peng** – State Key Laboratory of Polymer Materials Engineering, Polymer Research Institute of Sichuan University, Chengdu 610065, Sichuan, China

**Jingjing Jing** – State Key Laboratory of Polymer Materials Engineering, Polymer Research Institute of Sichuan University, Chengdu 610065, Sichuan, China

**Lu Yang** – State Key Laboratory of Polymer Materials Engineering, Polymer Research Institute of Sichuan University, Chengdu 610065, Sichuan, China

Complete contact information is available at:  
<https://pubs.acs.org/doi/10.1021/acssuschemeng.0c01877>

## Notes

The authors declare no competing financial interest.

## ■ ACKNOWLEDGMENTS

This work is financially supported by the National Key R&D Program of China (2017YFE0111500), the National Natural Science Foundation of China (51433006 and 51773121), the European Union's Horizon 2020-MSCA-RISE-734164 Graphene 3D Project, the Program of Innovative Research Team for Young Scientists of Sichuan Province (2016TD0010), and the Fundamental Research Funds for the Central Universities.

## ■ REFERENCES

- (1) Gibson, L. J.; Ashby, M. F. *Cellular Solids: Structure and Properties*; Cambridge University Press, 1999.
- (2) Kumar, S.; Ubaid, J.; Abishera, R.; Schiffer, A.; Deshpande, V. S. Tunable Energy Absorption Characteristics of Architected Honeycombs Enabled via Additive Manufacturing. *ACS Appl. Mater. Interfaces* **2019**, *11*, 42549–42560.
- (3) Bates, S. R. G.; Farrow, I. R.; Trask, R. S. 3D Printed Polyurethane Honeycombs for Repeated Tailored Energy Absorption. *Mater. Des.* **2016**, *112*, 172–183.
- (4) Lu, T.; Chen, C. Thermal Transport and Fire Retardance Properties of Cellular Aluminium Alloys. *Acta Mater.* **1999**, *47*, 1469–1485.
- (5) Freyman, T.; Yannas, I.; Gibson, L. Cellular Materials as Porous Scaffolds for Tissue Engineering. *Prog. Mater. Sci.* **2001**, *46*, 273–282.
- (6) Oh, J.-H.; Lee, H. R.; Umrao, S.; Kang, Y. J.; Oh, I.-K. Self-Aligned and Hierarchically Porous Graphene-Polyurethane Foams for Acoustic Wave Absorption. *Carbon* **2019**, *147*, 510–518.
- (7) Jiang, W.; Yan, L.; Ma, H.; Fan, Y.; Wang, J.; Feng, M.; Qu, S. Electromagnetic Wave Absorption and Compressive Behavior of a Three-Dimensional Metamaterial Absorber Based on 3D Printed Honeycomb. *Sci. Rep.* **2018**, *8*, 4817.
- (8) Yang, Y.; Song, X.; Li, X.; Chen, Z.; Zhou, C.; Zhou, Q.; Chen, Y. Recent Progress in Biomimetic Additive Manufacturing Technology: From Materials to Functional Structures. *Adv. Mater.* **2018**, *30*, 1706539.
- (9) Yeo, S. J.; Oh, M. J.; Yoo, P. J. Structurally Controlled Cellular Architectures for High-Performance Ultra-Lightweight Materials. *Adv. Mater.* **2019**, *31*, 1803670.
- (10) Schaedler, T. A.; Carter, W. B. Architected Cellular Materials. *Annu. Rev. Mater. Res.* **2016**, *46*, 187–210.
- (11) Compton, B. G.; Lewis, J. A. 3D-Printing of Lightweight Cellular Composites. *Adv. Mater.* **2014**, *26*, 5930–5935.
- (12) Kaur, M.; Han, S. M.; Kim, W. S. Three-Dimensionally Printed Cellular Architecture Materials: Perspectives on Fabrication, Material Advances, and Applications. *MRS Commun.* **2017**, *7*, 8–19.
- (13) Quan, Z.; Wu, A.; Keefe, M.; Qin, X.; Yu, J.; Suhr, J.; Byun, J.-H.; Kim, B.-S.; Chou, T.-W. Additive Manufacturing of Multi-Directional Preforms for Composites: Opportunities and Challenges. *Mater. Today* **2015**, *18*, 503–512.
- (14) Al-Ketan, O.; Soliman, A.; AlQubaisi, A. M.; Abu Al-Rub, R. K. Nature-Inspired Lightweight Cellular Co-Continuous Composites with Architected Periodic Gyroidal Structures. *Adv. Eng. Mater.* **2018**, *20*, 1700549.
- (15) Limmahakun, S.; Oloyede, A.; Sittiseripratip, K.; Xiao, Y.; Yan, C. 3D-Printed Cellular Structures for Bone Biomimetic Implants. *Addit. Manuf.* **2017**, *15*, 93–101.
- (16) Maurath, J.; Willenbacher, N. 3D Printing of Open-Porous Cellular Ceramics with High Specific Strength. *J. Eur. Ceram. Soc.* **2017**, *37*, 4833–4842.



- (17) Wang, X.; Jiang, M.; Zhou, Z.; Gou, J.; Hui, D. 3D Printing of Polymer Matrix Composites: A Review and Prospective. *Composites, Part B* **2017**, *110*, 442–458.
- (18) Campbell, T. A.; Ivanova, O. S. 3D printing of multifunctional nanocomposites. *Nano Today* **2013**, *8*, 119–120.
- (19) Abbasi, H.; Antunes, M.; Velasco, J. I. Recent Advances in Carbon-Based Polymer Nanocomposites for Electromagnetic Interference Shielding. *Prog. Mater. Sci.* **2019**, *103*, 319–373.
- (20) Chen, J.; Liao, X.; Xiao, W.; Yang, J.; Jiang, Q.; Li, G. Facile and Green Method To Structure Ultralow-Threshold and Lightweight Polystyrene/MWCNT Composites with Segregated Conductive Networks for Efficient Electromagnetic Interference Shielding. *ACS Sustainable Chem. Eng.* **2019**, *7*, 9904–9915.
- (21) Jia, L.-C.; Li, M.-Z.; Yan, D.-X.; Cui, C.-H.; Wu, H.-Y.; Li, Z.-M. A Strong and Tough Polymer-Carbon Nanotube Film for Flexible and Efficient Electromagnetic Interference Shielding. *J. Mater. Chem. C* **2017**, *5*, 8944–8951.
- (22) Shen, Z.; Feng, J. Preparation of Thermally Conductive Polymer Composites with Good Electromagnetic Interference Shielding Efficiency Based on Natural Wood-Derived Carbon Scaffolds. *ACS Sustainable Chem. Eng.* **2019**, *7*, 6259–6266.
- (23) Zhang, H.-B.; Zheng, W.-G.; Yan, Q.; Jiang, Z.-G.; Yu, Z.-Z. The Effect of Surface Chemistry of Graphene on Rheological and Electrical Properties of Polymethylmethacrylate Composites. *Carbon* **2012**, *50*, 5117–5125.
- (24) Ling, J.; Zhai, W.; Feng, W.; Shen, B.; Zhang, J.; Zheng, W. Facile Preparation of Lightweight Microcellular Polyetherimide/Graphene Composite Foams for Electromagnetic Interference Shielding. *ACS Appl. Mater. Interfaces* **2013**, *5*, 2677–2684.
- (25) Yan, D.-X.; Ren, P.-G.; Pang, H.; Fu, Q.; Yang, M.-B.; Li, Z.-M. Efficient Electromagnetic Interference Shielding of Lightweight Graphene/Polystyrene Composite. *J. Mater. Chem.* **2012**, *22*, 18772–18774.
- (26) Cui, C.-H.; Yan, D.-X.; Pang, H.; Xu, X.; Jia, L.-C.; Li, Z.-M. Formation of a Segregated Electrically Conductive Network Structure in a Low-Melt-Viscosity Polymer for Highly Efficient Electromagnetic Interference Shielding. *ACS Sustainable Chem. Eng.* **2016**, *4*, 4137–4145.
- (27) Zhao, X.; Zhang, Q.; Chen, D.; Lu, P. Enhanced Mechanical Properties of Graphene-Based Poly(vinyl alcohol) Composites. *Macromolecules* **2010**, *43*, 2357–2363.
- (28) Yang, X.; Fan, S.; Li, Y.; Guo, Y.; Li, Y.; Ruan, K.; Zhang, S.; Zhang, J.; Kong, J.; Gu, J. Synchronously Improved Electromagnetic Interference Shielding and Thermal Conductivity for Epoxy Nanocomposites by Constructing 3D Copper Nanowires/Thermally Annealed Graphene Aerogel Framework. *Composites, Part A* **2020**, *128*, 105670.
- (29) Kuester, S.; Demarquette, N. R.; Ferreira, J. C., Jr; Soares, B. G.; Barra, G. M. Hybrid Nanocomposites of Thermoplastic Elastomer and Carbon Nanoadditives for Electromagnetic Shielding. *Eur. Polym. J.* **2017**, *88*, 328–339.
- (30) Du, J.; Zhao, L.; Zeng, Y.; Zhang, L.; Li, F.; Liu, P.; Liu, C. Comparison of Electrical Properties between Multi-Walled Carbon Nanotube and Graphene Nanosheet/High Density Polyethylene Composites with a Segregated Network Structure. *Carbon* **2011**, *49*, 1094–1100.
- (31) Lin, J.-H.; Lin, Z.-I.; Pan, Y.-J.; Chen, C.-K.; Huang, C.-L.; Huang, C.-H.; Lou, C.-W. Improvement in Mechanical Properties and Electromagnetic Interference Shielding Effectiveness of PVA-Based Composites: Synergistic Effect Between Graphene Nano-Sheets and Multi-Walled Carbon Nanotubes. *Macromol. Mater. Eng.* **2016**, *301*, 199–211.
- (32) Jia, L.-C.; Yan, D.-X.; Jiang, X.; Pang, H.; Gao, J.-F.; Ren, P.-G.; Li, Z.-M. Synergistic Effect of Graphite and Carbon Nanotubes on Improved Electromagnetic Interference Shielding Performance in Segregated Composites. *Ind. Eng. Chem. Res.* **2018**, *57*, 11929–11938.
- (33) Liang, C.; Qiu, H.; Song, P.; Shi, X.; Kong, J.; Gu, J. Ultra-Light MXene Aerogel/Wood-Derived Porous Carbon Composites with Wall-Like “Mortar/Brick” Structures for Electromagnetic Interference Shielding. *Sci. Bull.* **2020**, *65*, 616–622.
- (34) Wang, L.; Qiu, H.; Song, P.; Zhang, Y.; Lu, Y.; Liang, C.; Kong, J.; Chen, L.; Gu, J. 3D Ti<sub>3</sub>C<sub>2</sub>T<sub>x</sub> MXene/C Hybrid Foam/Epoxy Nanocomposites with Superior Electromagnetic Interference Shielding Performances and Robust Mechanical properties. *Composites, Part A* **2019**, *123*, 293–300.
- (35) Shi, S.; Chen, Y.; Jing, J.; Yang, L. Preparation and 3D-Printing of Highly Conductive Polylactic Acid/Carbon Nanotube Nanocomposites via Local Enrichment Strategy. *RSC Adv.* **2019**, *9*, 29980–29986.
- (36) Spinelli, G.; Lamberti, P.; Tucci, V.; Ivanova, R.; Tabakova, S.; Ivanov, E.; Kotsilkova, R.; Cimmino, S.; Di Maio, R.; Silvestre, C. Rheological and Electrical Behaviour of Nanocarbon/Poly(lactic) Acid for 3D Printing Applications. *Composites, Part B* **2019**, *167*, 467–476.
- (37) Song, Y.; Zheng, Q. Linear Viscoelasticity of Polymer Melts Filled with Nano-Sized Fillers. *Polymer* **2010**, *51*, 3262–3268.
- (38) Du, F.; Scogna, R. C.; Zhou, W.; Brand, S.; Fischer, J. E.; Winey, K. I. Nanotube Networks in Polymer Nanocomposites: Rheology and Electrical Conductivity. *Macromolecules* **2004**, *37*, 9048–9055.
- (39) Zhang, S.; Yin, S.; Rong, C.; Huo, P.; Jiang, Z.; Wang, G. Synergistic Effects of Functionalized Graphene and Functionalized Multi-Walled Carbon Nanotubes on the Electrical and Mechanical Properties of Poly(ether sulfone) Composites. *Eur. Polym. J.* **2013**, *49*, 3125–3134.
- (40) Yue, L.; Pircheraghi, G.; Monemian, S. A.; Manas-Zloczower, I. Epoxy Composites with Carbon Nanotubes and Graphene Nanoplatelets-Dispersion and Synergy Effects. *Carbon* **2014**, *78*, 268–278.
- (41) Last, B.; Thouless, D. Percolation Theory and Electrical Conductivity. *Phys. Rev. Lett.* **1971**, *27*, 1719–1721.
- (42) Yang, W.; Gong, Y.; Zhao, X.; Liu, T.; Zhang, Y.; Chen, F.; Fu, Q. Strong and Highly Conductive Graphene Composite Film Based on the Nanocellulose-Assisted Dispersion of Expanded Graphite and Incorporation of Poly (ethylene oxide). *ACS Sustainable Chem. Eng.* **2019**, *7*, 5045–5056.
- (43) Hsiao, S. T.; Ma, C. C.; Tien, H. W.; Liao, W. H.; Wang, Y. S.; Li, S. M.; Yang, C. Y.; Lin, S. C.; Yang, R. B. Effect of Covalent Modification of Graphene Nanosheets on the Electrical Property and Electromagnetic Interference Shielding Performance of a Water-Borne Polyurethane Composite. *ACS Appl. Mater. Interfaces* **2015**, *7*, 2817–2826.
- (44) Feng, D.; Xu, D.; Wang, Q.; Liu, P. Highly Stretchable Electromagnetic Interference (EMI) Shielding Segregated Polyurethane/Carbon Nanotube Composites Fabricated by Microwave Selective Sintering. *J. Mater. Chem. C* **2019**, *7*, 7938–7946.